

HIGH-RESOLUTION MICROTOMOGRAPHY AND FAST RADIOGRAPHY FOR REAL-TIME AND IN-SITU CHARACTERIZATION OF POROUS MICROSTRUCTURES

T. Baumbach^{1,2}, L. Helfen^{1,3}, K. Schladitz⁴, P. Pernot^{2,3}, H. Stanzick⁵ and J. Banhart⁶

¹ Fraunhofer Institute for Nondestructive Testing (IZFP/EADQ), Dresden, Germany

² Institut für Synchrotronstrahlung, ANKA, Forschungszentrum Karlsruhe, Eggenstein-Leopoldshafen, Germany

³ European Synchrotron Radiation Facility (ESRF), Grenoble, France

⁴ Fraunhofer Institute for Industrial Mathematics (ITWM), Kaiserslautern, Germany

⁵ Fraunhofer Institute for Manufacturing and Advanced Materials (IFAM), Bremen, Germany

⁶ Hahn-Meitner-Institut, Berlin, Germany

Abstract: The potential of synchrotron-radiation imaging for non-destructive characterisation of material microstructure and its temporal evolution is demonstrated by the present study of metal foams. Synchrotron-radiation microtomography is applied to the study of statistical distribution properties at early foaming stages of the powder-metallurgical process for metal foam production. Image processing and analysis techniques yield quantitative results concerning pore nucleation and their early formation. This allows the investigation of similarities and differences of the metal foaming process with respect to the precursor material, its processing steps and process parameters.

Introduction: The investigation of structural properties of micro- and nanostructured materials is crucial for the understanding of their macroscopic properties and their formation. For micro- and nanostructured materials, *e.g.* foams, sponges or other porous materials such as cement, new experimental challenges — for instance the achievement of high spatial resolution and high sensitivity for different materials — are to be overcome. Nowadays, imaging with synchrotron radiation (SR) reaches spatial resolutions down to one micrometre in routine (see, *e.g.*, [1]) and down to the scale of some tens of nanometres in special exemplary cases (see, *e.g.*, [2]). Investigating the sample volume rather than merely the surface, SR imaging is therefore expected to complement the information necessary to the understanding of structural material properties obtained by established microscopy methods such as scanning electron microscopy.

In this paper we present a microtomographic study of metal foams. Due to relative densities $\eta = \rho_{por} / \rho_s$ (where ρ_{por} is the macroscopically determined mass density of the porous foam and ρ_s is the theoretical bulk density of the solid precursor material) up to a factor of one sixth, light-weight construction is one of the main interests for the application of solid foams made from metal, especially in the case of aluminium alloy foams. Moreover, the high energy dissipation per unit mass makes those foams attractive in ground transportation applications for increasing passenger safety in crash situations. Additionally, improved properties with respect to the bulk materials concerning acoustical and mechanical damping and heat conduction may be noted [3].

Depending on foam expansion, metal foams can have characteristic sizes and distances of their constituents on and below the micrometre scale. Modern x-ray laboratory computed tomography (CT) scanners are able to attain spatial resolutions down to approximately 10 μm which allows one to resolve the cell walls of aluminium alloy foams and thus to study the 3d structure [4] of expanded metal foams, *e.g.* under mechanical load [5]. Olurin *et al.* [6] acquired 3d data to determine morphological parameters of foam samples near full expansion.

Although nowadays the technology for metal foaming is rather well established, metal foam *formation* is still rather poorly explored. In this paper we demonstrate the application of synchrotron-radiation (SR) imaging to investigate metal foam formation. *In situ* observation of the foaming process under thermal load has already been performed by fast radiography. They were the first experiments which allowed the study of the internal foam structure during expansion under heat treatment. Results concerning foaming physics, the materials science aspects and concerning technological application have been published elsewhere [9,10,11,16].

In this paper, the application of synchrotron-radiation CT is reported to investigate series of foam samples in which each individual sample represents a particular expansion stage

corresponding to a certain foaming time. Three-dimensional (3d) image analysis techniques are used to quantify distribution properties of the 3d microstructure of such partly expanded foam samples. A comparison between the individual samples of the series yields information concerning pore nucleation and their early formation.

The samples investigated in this paper are produced by the *powder-metallurgical* (PM) method [3] which is described along with the experimental set-up for microtomography hereafter. Then we present results obtained by the experiments and by the applied image processing and analysis techniques. Finally, the conclusions subsume the results.

Nowadays there exists a variety of methods [3,12] for metal foam production. The two-step procedure of the PM production method is described in the following for a foam made of an aluminium alloy containing 7 wt-% of silicon (AlSi7). For the *production of a foamable precursor* three powders were used, namely powders of pure aluminium and of pure silicon to form an AlSi7 alloy matrix with the addition of 0.5 wt-% of a TiH₂ powder as blowing agent.

Subsequently, the powder blend was compacted to a foamable precursor material by conventional axial (closed-die) compression at a temperature of 450 °C and a pressure of 120 MPa. The resulting precursor material had low residual porosity ($\leq 0.75\%$) [9]. Extrusion would be an alternative powder compaction method [13] which is especially suited for industrial application. For the *production of the final metal foam*, the foaming process is triggered by heating the obtained precursor material within a pre-heated furnace. During the heating process the blowing agent TiH₂ decomposes and releases the blowing gas hydrogen. As a consequence pores form in the metal matrix and the sample expands. Furnace temperatures between 600 and 800 °C are usually employed for foaming Al alloys. Highest volume expansion during foaming can be expected at around 700 °C for AlSi7 precursor materials with 0.5 wt-% TiH₂ [13]. For technological application the foaming process is interrupted at its maximum expansion by quenching the sample, freezing in this way the foam structure.

Instead of the two base powders Al and Si forming the alloy we also use (as in the case of the aluminium alloy AA6061) one *pre-alloyed* powder. Pre-alloyed powders are more expensive and therefore less employed for technological applications. Moreover, pre-alloyed Al-Si alloy powders were found to exhibit a significantly worse foamability [14] than their counterpart based on two base powders.

In Fig. 1, a typical set-up used at ID19 for microtomography is sketched. The basic elements are the synchrotron source (at approx. 140 m distance), a monochromator, a rotation stage employed to turn the sample during the tomographic scan and the detector. The low beam divergence available at synchrotron sources permits the use of monochromator optics. Monochromatic radiation enables the quantitative reconstruction of the spatial distribution of the linear attenuation coefficient $\mu(x,y,z)$ for the selected x-ray energy, avoiding artefacts due to beam hardening. As a consequence the visibility of spatial features in the reconstructed image is improved for the identification of the blowing agent particles, alloy matrix and pores. For intermediate pixel sizes from approximately 5 μm onwards we usually employ a fixed-exit double-crystal monochromator with its 111 reflection of perfect silicon crystals. For higher imaging resolutions down to pixel sizes of 0.3 μm we use a high-bandwidth multilayer monochromator diffracting in a vertical plane.

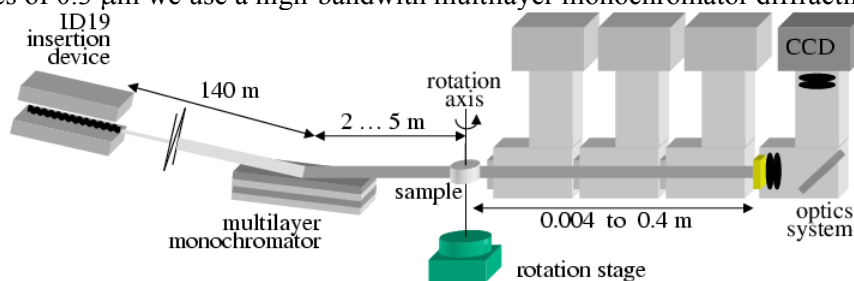


Figure 1: Sketch of the experimental set-up for microtomography at ID19 of the ESRF. For holographic tomography, radiographs exhibiting interference patterns due to Fresnel diffraction are recorded at different distances to the sample. The ESRF Frelon CCD camera as a basis for the electronic detector system.

Different effective pixel sizes of the acquired image can be realised by changing the optics unit composed of a scintillator screen or crystal, a visible-light magnifying or demagnifying optics system and a mirror.

Results: Reconstruction of the 3d distribution of the linear attenuation coefficient $\mu(x,y,z)$ from the acquired projection data sets is performed by a filtered-backprojection algorithm [15] for the parallel-beam case. In the following we will present examples for the application of absorption tomography — based on attenuation of the incident radiation — and for phase-contrast imaging — based on a distortion of the x-ray wavefront after passing the object.

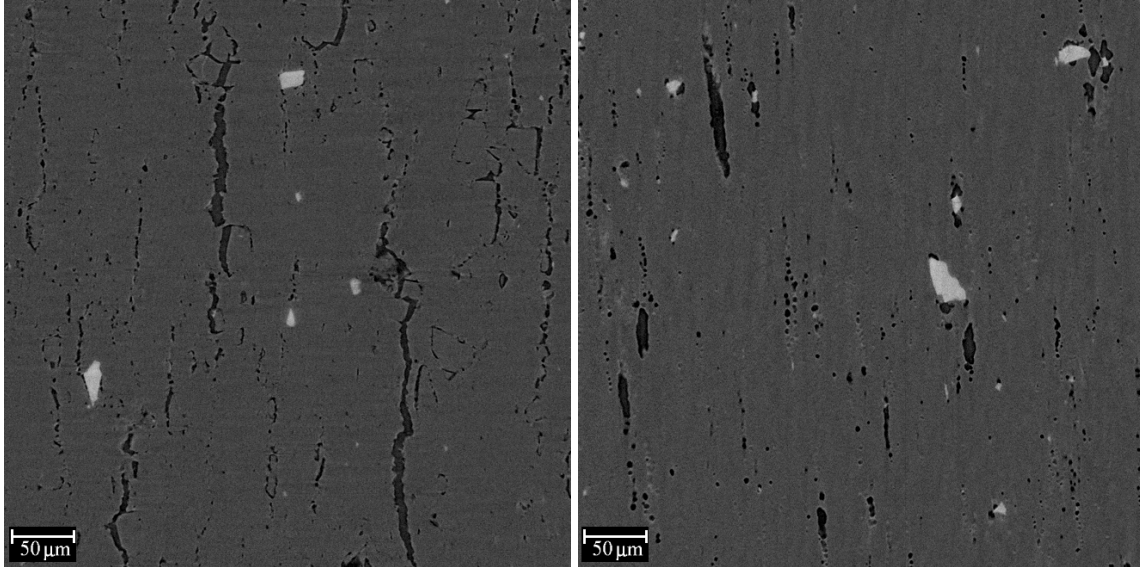


Figure 2: *Ex situ* microtomography: slices taken from the reconstructed 3d data sets. X-ray energy was 18 keV, image sizes are 660×660 voxels (voxel size 0.7 μm). The AlSi7 sample (left, macroscopic porosity $\varepsilon=0.09$) stems from a uniaxially compacted mix of Al and Si base powders whereas the AA6061 precursor (right, $\varepsilon=0.01$) was extruded from a pre-alloyed metal powder.

Fig. 2 gives an impression of the spatial resolution and image quality realisable by SR microtomography. Two reconstructed slices with 0.7 μm pixel size show different precursor materials shortly after the onset of foaming, *i.e.* with macroscopically determined porosities $\varepsilon < 0.1$.¹ Pores are rendered black, the alloy matrix in dark grey and highly absorbing blowing agent particles in light grey. In both reconstructed slices, the principal compaction direction (of the powder mix) is oriented horizontally. The pore morphology is quite different between the two materials: for AlSi7, irregular crack-like voids are observed whereas for AA6061 they are more regularly shaped. Moreover, for AlSi7 the blowing agent particles do not seem to be spatially correlated with the pores whereas for AA6061 they are often found close to the pores. The choice of the 2d slice through the 3d volume, however, might not cut a pore which is adjacent to a blowing agent particle or *vice versa*. But indeed, using 3d image processing and analysis techniques, a strong (“true”) spatial correlation between blowing agent and pores was determined [16] for the AA6061 sample while no significant spatial correlation was found for AlSi7.

The 3d renditions given in the top row of Fig. 3 visualise the change of the morphology of the pore structure during foam expansion. Already in the solid state, fissure-like pores form up in the metallic matrix. The fissures are spatially extended perpendicular with respect to the principal powder compaction axis. This also results in a directionality of foam rise. In comparison to other precursor materials, the shown samples made from a pre-alloyed AA6061 metal powder exhibit a rather homogeneous pore formation throughout the entire volume. The morphology of the metal matrix up to $\varepsilon=0.44$ resembles “split wood” with solid “fibres” crossing rod-like or lens-like pores.

¹The macroscopically determined porosity $\varepsilon=1-\eta$ (with η the relative density) is used in the following as a measure to describe the expansion stage.

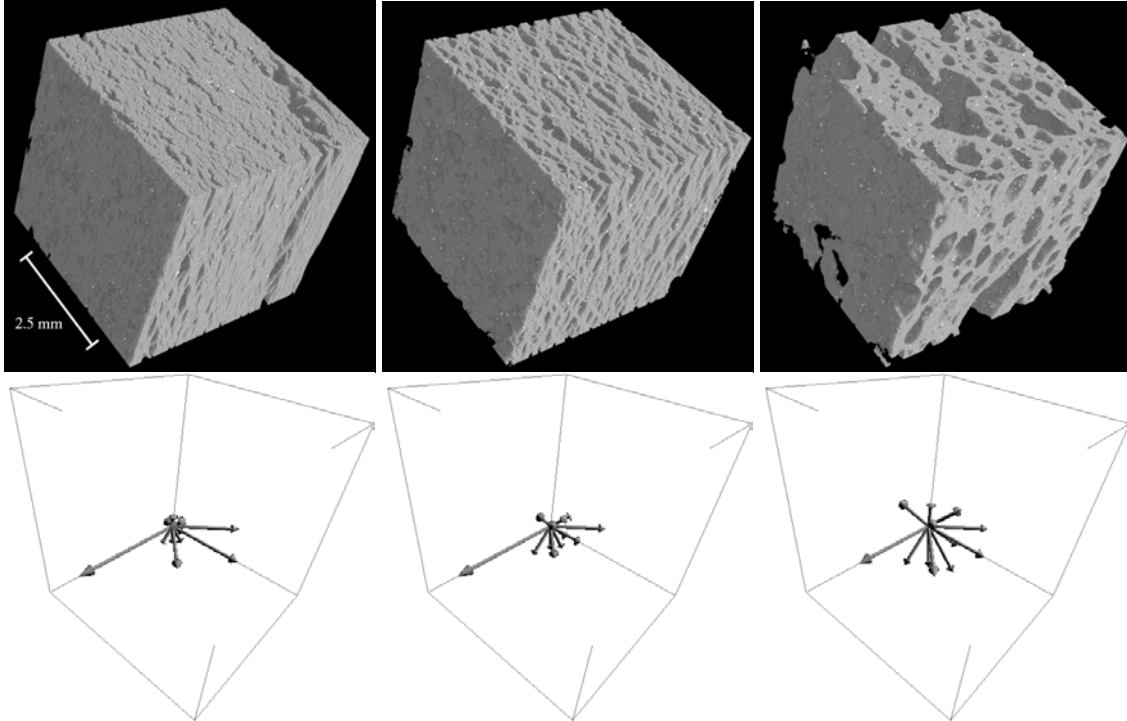


Figure 3: Top row: 3d renditions of different foam expansion stages for the AA6061 series (from left to right: $\varepsilon=0.30, 0.44, 0.56$). The pore space is rendered transparent, the alloy matrix is grey and the remnants (mainly Ti) of the blowing agent particles are the light spots. Voxel size is $6.7 \mu\text{m}$. Bottom row: corresponding (discrete) directional distributions of the mean surface of the pore space.

In order to investigate the evolution of pore morphology of this sample series quantitatively, we analyse the 3d images with respect to the volume fraction and the mean surface distribution of the pore space. Measurement of data is based on segmented [17] binary images of microstructural constituents representing the spatial distribution of the blowing agent (the TiH_2 particles) and the solid matter (the entire metallic matrix), respectively. The measurement of the volume fraction of the pores is based on counting of the voxels of the binary image concerning the pore space. For the measurement of the specific surface area an integral-geometric approach is applied [16]. For details of the mathematical and numerical methods the reader is referred to [18,19].

alloy	pixel size	macrosc. porosity ε	computed porosity	specific surface area in m^{-1}
AlSi7	$0.7 \mu\text{m}$	0.09	0.049	68053.8
AA6061	$0.7 \mu\text{m}$	0.01	0.027	34219.1
AA6061	$6.7 \mu\text{m}$	0.30	0.312	25381.9
AA6061	$6.7 \mu\text{m}$	0.44	0.407	16689.1
AA6061	$6.7 \mu\text{m}$	0.56	0.549	7721.3

Table 1: Computed characteristics of porosity and specific surface area of the pore space for the samples of macroscopic porosity ε .

In Table 1 the volume fractions and specific surface areas of the pore space are given for the various expansion stages. With increasing foam expansion, the specific surface area of the pore space decreases since the pores inflate and transform after appearance of the liquid state from “split-wood”-like to a rounder, almost spherical shape (see top row of Fig. 3).

The directional distribution of the mean surface is approximated by a discrete distribution on the unit sphere (see bottom row of Fig. 3). The lengths of the arrows shown in the diagrams is proportional to the fraction of surface normal vectors corresponding to the arrows’ directions. The two longest arrows of the top diagram correspond to the already noted rod-like pore shapes at $\varepsilon=0.30$: almost no surface is oriented perpendicular to these two arrows (parallel to the up-down

direction of the 3d rendition). The texture introduced by the powder compaction process (here extrusion) results in the observed strong biaxiality of the mean surface distribution. The extrusion process is characterised by a principal and a secondary compression axis which are defined by the aspect ratio of the extruded product of $160 \times 20 \text{ mm}^2$ rectangular section. The longest arrow of each diagram is parallel to the principal axis of precursor compaction. In the second expansion stage $\varepsilon=0.44$ the part of the surface with its normal oriented parallel to the principal compaction direction clearly dominates but with increasing expansion this dominance reduces considerably as the pores attain a more spherical shape. In summary, at early foaming stages the anisotropic pore morphology closely reflects the texture induced by the powder compaction step. With proceeding foam expansion, surface tension appearing in the semi-liquid state is thought to reduce gradually this anisotropy.

From the point of view of material science, information concerning the percolation of the pore space is very important. In the case of the early foaming stages of metal foams a high degree of percolation of the pore space would enable the blowing gas hydrogen to escape from the evolving foam and thus not contribute to the formation of porosity.

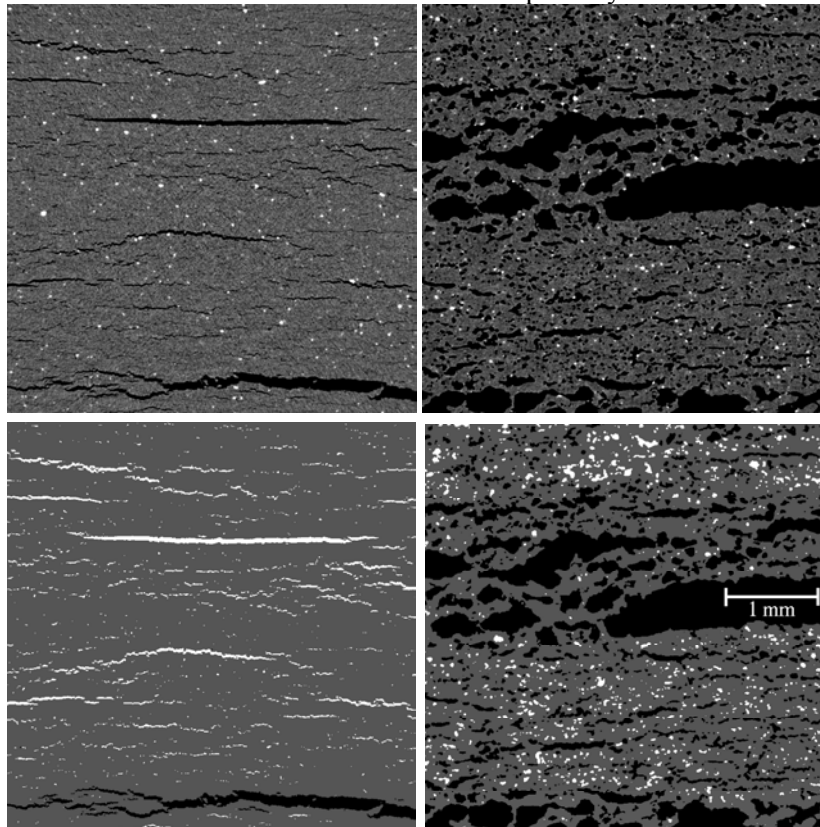


Figure 4: Top: reconstructed slices of a partly expanded AlSi7 foam with porosity $\varepsilon=0.09$ (left) and $\varepsilon=0.32$ (right). Pixel size is $6.7 \mu\text{m}$, image width 660 pixels. Bottom: corresponding partition (performed on the 3d images) of the network of pores into the volume belonging to the largest pore (black) and the remaining smaller pores (white). Please note that unlike in top two images the blowing agent is shown in the same grey value as the alloy matrix, namely dark grey, and therefore cannot be distinguished.

The image processing techniques *segmentation* and *labelling* are applied to yield the connected regions of the pore space, as performed on the reconstructed 3d images of partly foamed AlSi7 foams in the bottom images of Fig.4. At the first expansion stage $\varepsilon=0.09$ the largest pore consumes about 33 percent of the entire porosity. With increasing sample porosity the fraction of porosity occupied by the largest pore increases up to more than 87 percent for the expansion stage $\varepsilon=0.32$. The partitions of the largest pores are shown in Fig. 4 (bottom images) in comparison to the reconstructed images (top images). In the bottom images, the AlSi7 matrix and blowing agent are rendered in dark grey, black denotes the largest pore and white all remaining

pores. For $\epsilon=0.09$ the largest pore is spatially rather confined in the position on the vertical axis in the image, to which the powder compression axis was parallel. Obviously, in the case of $\epsilon=0.32$, the pores which are elongated in the horizontal direction of the image tend in 3d to be a member of the largest pore whereas small pores with a less oblate shape do in general not belong to it. In other words, the largest pores forms a network of interconnected pores / cracks of a labyrinth-like structure which is surrounded by smaller pores with a rounder shape. It can be concluded that the blowing gas hydrogen would escape from the expanding foam structure through such pore networks and not contribute to the formation of porosity.

Up to now, the distinction between materials of only slightly different absorption coefficient is an unsolved problem for laboratory CT. Using monochromatic radiation and the high partial coherence provided by synchrotron-radiation imaging set-ups, the modulation of the amplitude and the phase of the x-ray wavefield emerging the sample can be retrieved. This so-called holographic CT is based on the acquisition of x-ray interference images due to Fresnel diffraction at different detector-to-sample distances. To a good approximation, the spatial electron density distribution within the sample can be reconstructed [1,7].

Especially in Al-Si precursor materials made from two elemental base powders (e.g. an aluminium powder mixed with 7 wt-% silicon powder for the alloy AlSi7) the Si powder particles can be distinguished from the solid matrix. For the following example, tomographic scans (using the sample rotation θ) were acquired at different detector-sample distances $z= 0.004, 0.064, 0.154$ and 0.4 m (referring to the experimental set-up at ID19 sketched in Fig. 1).

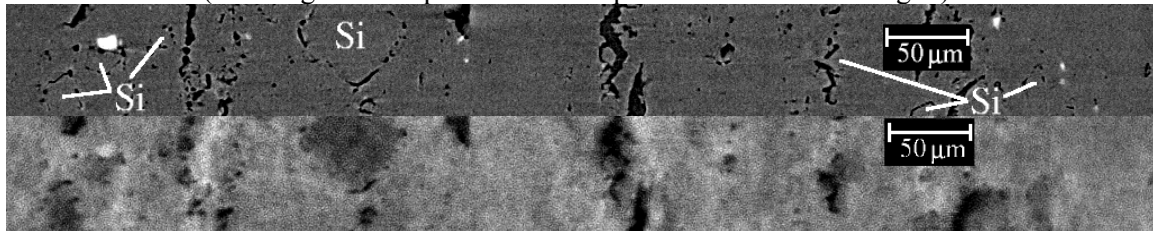


Figure 5: Cross-sectional images (see text) through a partly expanded Al-Si foam samples ($\epsilon= 0.09$), reconstructed from 1400 projection directions at an x-ray energy of 18 keV. For both images pores are rendered black, the blowing agent TiH_2 white. In the holographically reconstructed image (bottom), silicon particles can be identified from the aluminium matrix as the darker grey regions. In the absorption image (top) these particles (labeled by “Si”) cannot be distinguished from the surrounding matrix. Pixel size is $0.7 \mu m$, image width 512 pixels.

Fig. 5 displays reconstructed cross-sectional slices of both the absorption (using only the smallest detector-sample distance) and the holographically reconstructed image (using the information from all detector-sample distances) for one early expansion stage of AlSi7. Pores are rendered in black, the blowing agent in white and the alloy matrix in the remaining grey values. While the Si particles are not discernible in the absorption image, the holographically reconstructed image clearly displays them as the darker grey regions. From a comparison between the two images it can be concluded that among the pores visible there are a some of them in direct neighbourhood to Si particles whereas little or no spatial correlation with respect to the blowing agent is evident.

The distinction between silicon particles from the solid matrix opens the possibility to investigate non-destructively the pore nucleation process in the sample volume for different precursor materials. Different nucleation mechanisms can thus be identified. In summary, for the two precursor materials treated above, the following conclusions can be drawn [20]: AA6061 made from one pre-alloyed base powder exhibits predominantly local pore nucleation correlated to the blowing agent particles while AlSi7 made from two base powders the pores nucleate predominantly in the surroundings of silicon powder particles. This agrees with results of 3d image analysis on such early Al-Si foam expansion stages made from two base powders [16] where no significant spatial correlation between blowing agent particles and pores was found. Instead, pores initiate predominantly near the Si particles.

Conclusions: Tomographic experiments image the sample volume non-destructively in 3d. At the sample interior, the sample preparation has no detrimental effect on the constituents (*i.e.* the blowing agent particles). The application of SR yields highly contrasted reconstructions since monochromatic radiation permits the quantitative determination of the linear attenuation coefficient distribution and reduces reconstruction artefacts. Thus the pores, alloy matrix and blowing agent could be separated with high spatial resolution down to the scale of one micrometre. Dedicated 3d image processing and analysis techniques can give access to the statistical distribution properties among sample series. In particular, the pore–matrix interface could be examined quantitatively which allows us to draw conclusions on the time evolution of pore morphology during foaming. In the solid state, pore morphology closely reflects the anisotropic strength of the precursor material which is a result of the powder compaction step. A network of pores develops which is thought to be the consequence of crack merging and allow a part of the blowing gas to escape from the expanding foam structure. After the transition to the semi-solid state, surface tension becomes dominant which reduces gradually the observed anisotropic pore morphology and enables a closing of open-porous crack networks.

Moreover, similarly absorbing materials could be distinguished by holographic imaging. Different crack nucleation mechanisms could thus be identified for two differently produced precursor materials, one of them containing silicon powder particles, the other none.

In summary, pore nucleation and formation can be related by the described investigation methods to the precursor material, its production steps and process parameters.

References:

- [1] P. Cloetens, W. Ludwig, J. Baruchel, D. van Dyck, J. van Landuyt, J.P. Guigay, and M. Schlenker. Holotomography: Quantitative phase tomography using coherent synchrotron radiation. *Appl. Phys. Lett.*, 75: 2912, 1999.
- [2] U. Neuhäusler, G. Schneider, W. Ludwig, M.A. Meyer, E. Zschech, and D. Hambach. X-ray microscopy in Zernike phase contrast mode at 4 keV photon energy with 60 nm resolution. *J. Phys. D: Appl. Phys.*, 36: A79–A82, 2003.
- [3] J. Banhart. Manufacture, characterisation and application of cellular metals and metal foams. *Progr. Mater. Sci.*, 46: 559–632, 2001.
- [4] A. Sassov. Non-destructive 3-d investigation of metallic foam microstructures. *Adv. Eng. Mater.*, 2: 466–470, 2000.
- [5] H. Bart-Smith, A.-F. Bastawros, D.R. Mumm, A.G. Evans, D.J. Sypeck, and H.N.G. Wadley. Compressive deformation and yielding mechanisms in cellular Al alloys determined using x-ray tomography and surface strain mapping. *Acta Mater.*, 46: 3582–3592, 1998.
- [6] O.B. Olurin, M. Arnold, C. Körner, and R.F. Singer. The investigation of morphometric parameters of aluminium foams using micro-computed tomography. *Materials Science and Engineering A*, 328: 334–343, 2002.
- [7] P. Cloetens, W. Ludwig, E. Boller, L. Helfen, L. Salvo, R. Mache, and M. Schlenker. Quantitative phase contrast tomography using coherent synchrotron radiation. In U. Bonse, editor, *Proceedings SPIE: Developments in X-Ray Tomography III*, volume 4503, pages 82–91, 2002.
- [8] T. Weitkamp, C. Rau, A. Snigirev, B. Benner, T.F. Günzler, M. Kuhlmann, and C.G. Schroer. Phase contrast in synchrotron-radiation microradiography and tomography. In U. Bonse, editor, *Proceedings SPIE: Developments in X-Ray Tomography III*, volume 4503, pages 92–102, 2002.
- [9] J. Banhart, H. Stanzick, L. Helfen, and T. Baumbach. Metal foam evolution studied by synchrotron radiography. *Appl. Phys. Lett.*, 78: 1152–1154, 2001.
- [10] J. Banhart, H. Stanzick, L. Helfen, T. Baumbach, and K. Nijhof. Real-time x-ray investigation of aluminium foam sandwich production. *Adv. Eng. Mater.*, 3: 407, 2001.

- [11] H. Stanzick, M. Wichmann, J. Weise, L. Helfen, T. Baumbach, and J. Banhart. Process control in aluminium foam production using real-time x-ray radioscopy. *Adv. Eng. Mater.*, 4(10): 814–823, 2002.
- [12] C. Körner and R.F. Singer. Processing of metal foams — challenges and opportunities. *Adv. Eng. Mater.*, 2: 159–165, 2000.
- [13] I. Duarte and J. Banhart. A study of aluminium foam formation — kinetics and microstructure. *Acta Mater.*, 48: 2349–2362, 2000.
- [14] B. Kriszt, P. Cekan, and K. Faure. Foamability of the Al-Si system. In J. Banhart, M. Ashby, and N. Fleck, editors, *Cellular Metals and Metal Foaming Technology*, pages 77–82, 2001.
- [15] G. T. Herman. *Image Reconstruction from Projections*. Academic Press, New York, 1980.
- [16] L. Helfen, H. Stanzick, J. Ohser, K. Schladitz, P. Pernot, J. Banhart, and T. Baumbach. Investigation of the foaming process of metals by synchrotron-radiation imaging. In N. Meyendorf, G.Y. Baaklini, and B. Michel, editors, *Proceedings SPIE: Testing, Reliability, and Application of Micro- and Nanomaterial Systems*, volume 5045, pages 254–265 (in press), 2003.
- [17] K.R. Castleman. *Digital image processing*. Prentice-Hall International Inc., Englewood Cliffs, New Jersey, 1996.
- [18] J. Ohser and F. Mücklich. *Statistical Analysis of Microstructures in Materials Science*. J Wiley & Sons, Chichester, New York, 2000.
- [19] C. Lang, J. Ohser, and R. Hilfer. On the analysis of spatial binary images. *J. Microsc.*, 202: 1–12, 2001.
- [20] L. Helfen, P. Cloetens, P. Pernot, H. Stanzick, J. Banhart, and T. Baumbach. , to be published.